Manipulating elastic waves via engineered spatial curvature profiles

Matteo Mazzotti, Mohit Gupta, Christian Santangelo, Massimo Ruzzene

Matteo Mazzotti, Mohit Gupta, Christian Santangelo, Massimo Ruzzene, "Manipulating elastic waves via engineered spatial curvature profiles," Proc. SPIE 12048, Health Monitoring of Structural and Biological Systems XVI, 1204804 (19 April 2022); doi: 10.1117/12.2612573

SPIE.

Event: SPIE Smart Structures + Nondestructive Evaluation, 2022, Long Beach, California, United States

Manipulating elastic waves via engineered spatial curvature profiles

Matteo Mazzotti[a], Mohit Gupta[a], Christian Santangelo[b], and Massimo Ruzzene[a]

[a]Department of Mechanical Engineering, University of Colorado Boulder, 1111 Engineering Dr, UCB 427, Boulder, USA
[b]Department of Physics, Syracuse University, 229G Physics Building, Syracuse, USA

ABSTRACT

We investigate curved surfaces operating as geodesic lenses for elastic waves. Consistently with findings in optics, we show that wave propagation occurs along rays that correspond to the geodesics of the curved surfaces, and we establish the geometric equivalence between Gaussian curvature and refractive index. This equivalence is formulated for flexural waves in curved shells by showing that, in the short wavelength limit, the ray equation corresponds to the classical equation of geodesics. We leverage this result to identify a non-Euclidean transformation that maps the geometric profile of a isotropic curved waveguide into a spatially varying refractive index distribution for a planar waveguide. These theoretical predictions are validated first through numerical simulations, and subsequently through experiments on 3D printed curved membranes with different curvature distributions. Numerical and experimental findings confirm that focal regions and caustic networks are correctly predicted based on geodesic evaluations. Our results form the basis for the design of curved profiles that correspond to spatial distributions of the refractive index and induce focal points by forcing waves to propagate along predefined trajectories. The findings of this study also suggest curvature as an attractive alternative to strategies based on the local tailoring of material properties and geometrical patterns that have gained in popularity for gradient-index lens design.

Keywords: Elastic waves, curved waveguides, geodesics, ray tracing, refractive index, Gaussian curvature, non-Euclidean transformations, 3D printing

1. INTRODUCTION

In recent years, non-Euclidean transformations[1,2] have been proposed as an alternative approach to Transformation Optics (TO)[3,4] and metamaterial concepts[5–8] for the implementation of optical lenses and the realization of exotic waveguiding effects. While TO is based on a spatial modulation of the refractive index that follows from the geometric distortion induced on a planar waveguide,[1,9–12] non-Euclidean transformations seek to transform a gradient refractive index (GRIN) planar surface into a curved one in which the variation of the refractive index is recovered by the local surface curvature. This approach also allows to mimic anisotropic or singular distributions of the refractive index by allowing a flat waveguide to deform along its out-of-plane direction. This property, however, also poses a limit to the applicability of non-Euclidean transformations, which can only be applied between flat and curved two-dimensional spaces.

The origin of non-Euclidean transformations can be tracked back to Rinehart,[13,14] who first proposed an approach for the construction of the geodesic equivalent of a planar Luneburg lens. On the basis of this result, the geodesic Luneburg lens was further investigated in several other studies,[15–18] while similar approaches have also been proposed for the implementation of Maxwell fish-eye and Eaton lenses through the combination of curved surfaces and non-singular, isotropic refractive index distributions.[2,18–20]

Although non-Euclidean transformations have seen a considerable development in the fields of optics and electromagnetism, making possible the realization of non-conventional devices such as conformal optical devices for perfect imaging[21,22] and multibeam antennae,[23,24] their application in the field of elastic wave propagation

Further author information: (Send correspondence to Matteo Mazzotti)
E-mail: matteo.mazzotti@colorado.edu

Health Monitoring of Structural and Biological Systems XVI, edited by Paul Fromme, Zhongqing Su, Proc. of SPIE Vol. 12048, 1204804 · © 2022 SPIE
0277-786X · doi: 10.1117/12.2612573

has been limited so far to few studies only. For instance, in Ref. 25 it was demonstrated that the curvature of thin shells undergoing a flexural wave motion acts as a local index of refraction, and interfaces between positive and negative Gaussian curvature can lead to total internal reflection. In Ref. 26, it was shown that the two-dimensional analogous of a wormhole for flexural waves can be attained using a thin curved plate fabricated from homogeneous isotropic materials, and that an effective gradient index profile can be achieved merely by geometric curvature, even if reaches extreme values.

All the previously mentioned studies in optics and elasticity consider rotationally symmetric structures, while a gap exist in the current literature concerning non-Euclidean transformations for two-dimensional waveguides with a generic curvature or refractive index distribution. The objective of this work is to theoretically and experimentally investigate such waveguides. Specifically, we demonstrate that the governing equations of flexural waves in curved elastic waveguides reduce to the classical equation of geodesics in the geometrical optics limits, and we establish a non-Euclidean mapping that enables their study on a geometrically equivalent GRIN planar surface by means of ray analysis. Numerical and experimental results on Luneburg and Eaton lenses, as well as spatially modulated Gaussian profiles, indicate that our theoretical framework can be used in the design of generic two-dimensional curved surfaces capable of wave guiding and focusing without the need to resort to complex materials and fabrication processes.

2. THEORETICAL BACKGROUND

In this section, we first demonstrate that, in the short wavelength limit, the equation of flexural waves propagating in thin isotropic waveguides with generic curvature degenerates to the classical equation of geodesics. Using this result, we then illustrate how curvature can be exploited to design curved waveguides that mimic GRIN planar waveguides. To this end, we refer to Fig. 1, showing a planar waveguide of variable refractive index $n(x^1, x^2)$ whose midsurface S lies on the Euclidean plane x^1x^2, and a curved isotropic waveguide M whose midsurface elevation with respect to the same plane is described by the function $h(x^1, x^2)$. For the purpose of this work, we restrict the analysis to the case of a Monge patch, i.e. $h(x^1, x^2)$ is a continuous and differentiable function.

2.1 Geodesic Approximation of Flexural Wave Paths in the Short Wavelength Limit

We consider the propagation of flexural waves on M, on which an infinitesimal path ds is defined, using the formalism of differential geometry, by the metric

$$ds^2 = g_{\alpha\beta}dx^\alpha dx^\beta, \quad \alpha, \beta = 1, 2, \tag{1}$$

where $g_{\alpha\beta}$ denotes the covariant metric tensor. For a Monge patch, $g_{\alpha\beta}$ takes the form

$$g_{\alpha\beta} = \delta_{\alpha\beta} + \partial_\alpha h \partial_\beta h, \tag{2}$$

in which $\delta_{\alpha\beta}$ is the Kronecker's delta. Following the analysis in Refs. 27, 28, the propagation of flexural waves is assumed to satisfy the short wavelength limit $|k| \gg (rt)^{-1/2}$, where t is the constant thickness of the waveguide, r indicates the characteristic radius of curvature[29] and $k = (k_\alpha g^{\alpha\beta} k_\beta)^{1/2}$ the wavenumber, being $g^{\alpha\beta}$ the contravariant metric tensor. In this limit, the ray equations can be obtained as the trajectories of the Hamiltonian[27]

$$H = \frac{1}{2\omega}\frac{c_p^2 t^2}{12}\left[k_\alpha(s) g^{\alpha\beta}(x(s)) k_\beta(s)\right]^2, \tag{3}$$

in which ω denotes the circular frequency and $c_p = \omega/k$ the phase velocity of the flexural wave. Using Eq. (3) and the first fundamental relation of Hamiltonian dynamics $\dot{x}^\alpha(s) = \partial H/\partial k^\alpha$, we obtain the wavenumber

$$k_\alpha = \left(\frac{3\omega}{c_p^2 t^2}\right)^{1/3} \frac{g_{\alpha\beta}\dot{x}^\beta}{(\dot{x}^2)^{1/3}}. \tag{4}$$

which can be substituted into the second fundamental relation of Hamiltonian dynamics $\dot{k}^\alpha(s) = -\partial H/\partial x^\alpha$ along with $v^\beta \equiv \dot{x}^\beta/(\dot{x}^2)^{1/3}$, leading to

$$2\frac{1}{(\dot{x}^2)^{1/3}} g_{\gamma\beta}\dot{v}^\beta + 2\partial_\alpha g_{\gamma\beta} v^\alpha v^\beta - \partial_\gamma g_{\alpha\beta} v^\alpha = 0, \tag{5}$$

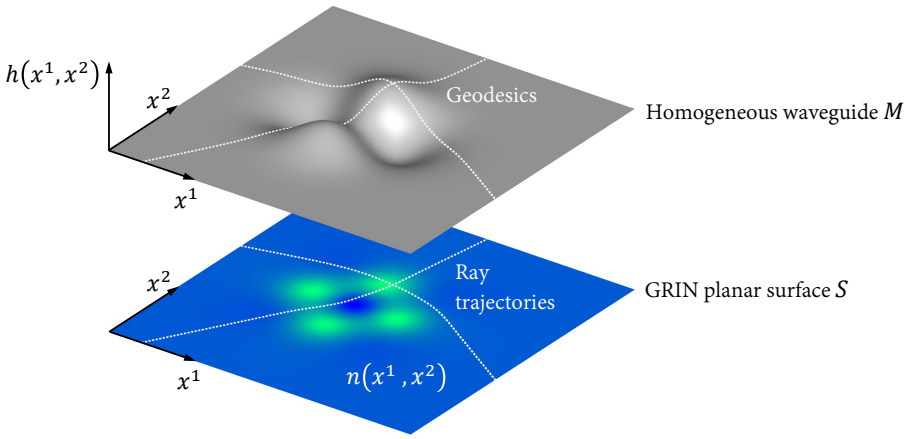

Figure 1. Mathematical model of the GRIN planar surface S and the geometrically equivalent homogeneous waveguide M.

where the temporal dependence is eliminated. Substituting $x^\alpha(s)$ back in Eq. (5), we finally obtain

$$\frac{1}{(\dot{x}^2)^{1/3}}\frac{d}{ds}\left(\frac{\dot{x}^\mu}{(\dot{x}^2)^{1/3}}\right)+\Gamma^\mu_{\ \alpha\beta}\left(\frac{\dot{x}^\alpha}{(\dot{x}^2)^{1/3}}\right)\left(\frac{\dot{x}^\beta}{(\dot{x}^2)^{1/3}}\right)=0, \tag{6}$$

which corresponds to the equation of geodesics when $\dot{x}_\alpha g^{\alpha\beta}\dot{x}_\beta = 1$. In Eq. (6), $\Gamma^\mu_{\ \alpha\beta}$ denote the Christoffel symbols of the second kind, which are defined as

$$\Gamma^\mu_{\ \alpha\beta}=\frac{1}{2}g^{\mu\nu}\left(\partial_\alpha g_{\beta\nu}+\partial_\beta g_{\alpha\nu}-\partial_\nu g_{\alpha\beta}\right). \tag{7}$$

Eq. (6) indicates that, in the geometrical optics limits, flexural rays traveling at constant phase speed c_p move along trajectories defined by geodesics. However, it is noted that the curvature of M induces, in general, small variations of the phase velocity at a given frequency ω.[30] Such variations are here considered negligible under the assumption $\lambda/r \ll 1$, where λ indicates the operative wavelength. Consequently, we assume the surface M to have a unit refractive index, and that the local variation of the ray trajectory due to a change of phase speed on S is entirely recovered by the local curvature on M. The relation between the refractive index and the Gaussian curvature is described in Section 2.2.

2.2 Geometric Equivalence Between Curved and GRIN Planar Waveguides

Starting from the fundamental result obtained in Section 2.1, we seek a transformation such that a projection of a ray path from M onto the Euclidean plane S with refractive index $n(x, y)$ coincides with that of a ray traveling along the plane itself. From Eq. (6), the wave trajectory is described on M by the equation of geodesics,

$$\frac{d^2x^\mu}{ds^2}+\Gamma^\mu_{\ \alpha\beta}\frac{dx^\alpha}{ds}\frac{dx^\beta}{ds}=0. \tag{8}$$

On the GRIN planar waveguide S, the path length da is related to the Euclidean metric $dl^2 = dx^2 + dy^2$ through $da^2 = n^2 dl^2$, while the wave trajectory is given by the solution of the ray equation[31]

$$\frac{d}{dl}\left(n\frac{dx^\alpha}{dl}\right)=\frac{\partial n}{\partial x^\alpha}. \tag{9}$$

By analogy with conformal transformations in optics,[2,32] S and M are geometrically equivalent if Fermat's principle applies along trajectories of waves having the same source coordinate (x^1, x^2) and direction ϑ, with $\cos\vartheta = \partial x^1/\partial s$ and $\sin\vartheta = \partial x^2/\partial s$. Thus, we require that the path lengths on M and S coincide, yielding

$$da^2 = ds^2 = g_{\alpha\beta}dx^\alpha dx^\beta = n^2\delta_{\alpha\beta}dx^\alpha dx^\beta. \tag{10}$$

If the metric tensor is given in isothermal coordinates (u, v), then from Eq. (10) one can easily deduce that $g_{uv} = \phi^2\delta_{uv}$ and $n^2 = \phi^2$, being $\phi(u, v)$ the conformal factor of M.[32,33] However, (x^1, x^2) are usually not isothermal for a Monge patch, and the direct application of Eq. (10) would first require the computation of the conformal factor of M in the isothermal parameterization (u, v) and then, in analogy with TO, an additional coordinate transformation for the refractive index from (u, v) back to (x^1, x^2). The computation of the conformal factor can be avoided by expressing both the refractive index $n(x^1, x^2)$ and geometric profile $h(x^1, x^2)$ as a function of the Gaussian curvature $K(x^1, x^2)$, which is an intrinsic measure of a surface that does not depend on its reparameterization. Using Eqs. (7) and (10) the Christoffel symbols of the second kind can be expressed in terms of the refractive index as[32]

$$\Gamma^{\mu}{}_{\alpha\beta} = \frac{1}{n}\left(\frac{\partial n}{\partial x^{\beta}}\delta_{\mu\alpha} + \frac{\partial n}{\partial x^{\alpha}}\delta_{\mu\beta} - \frac{\partial n}{\partial x^{\mu}}\delta_{\alpha\beta}\right). \tag{11}$$

Eq. (11) can be substituted in Ricci's tensor[32,33]

$$R_{\alpha\beta} = \partial_{\mu}\Gamma^{\mu}{}_{\alpha\beta} - \partial_{\beta}\Gamma^{\mu}{}_{\alpha\mu} + \Gamma^{\mu}{}_{\alpha\beta}\Gamma^{\nu}{}_{\mu\nu} - \Gamma^{\mu}{}_{\alpha\nu}\Gamma^{\nu}{}_{\mu\beta} \tag{12}$$

to express Gaussian curvature[32] $K = \frac{1}{2}g^{\alpha\beta}R_{\alpha\beta}$ in terms of refractive index. Since $g^{\alpha\beta} = n^{-2}\delta_{\alpha\beta}$, from Eqs. (11) and (12) we have

$$K = \frac{R_{\alpha\alpha}}{n^2} = \frac{1}{2} - \frac{\partial_{\alpha}\partial_{\alpha}n}{n^3} + \frac{(\partial_{\alpha}n)^2}{n^4}. \tag{13}$$

Finally, using the definition of $K(x^1, x^2)$ for Monge patches,[34] we obtain

$$-\frac{\nabla\cdot\nabla n}{n^3} + \frac{\nabla n\cdot\nabla n}{n^4} = \frac{\det\left[\partial^2 h/\partial x^{\alpha}\partial x^{\beta}\right]}{\left[1+(\nabla h\cdot\nabla h)\right]^2}, \tag{14}$$

which defines a local mapping between the refractive index $n(x^1, x^2)$ and the surface elevation $h(x^1, x^2)$ through the Gaussian curvature $K(x^1, x^2)$. Eq. (14) can be regarded as the two-dimensional generalization of the non-Euclidean transformation described in Refs. 2, 19, 20, where graded index lenses are mapped onto rotationally symmetric curved surfaces. A similar result was also presented for one-dimensional problems in Ref. 35 to study mirages with vanishing and constant Gaussian curvature when the refractive index of the atmosphere is a function of the altitude only.

3. NON-EUCLIDEAN TRANSFORMATIONS

In this Section, we illustrate the concept of geometric equivalence between refractive index and Gaussian curvature through numerical analyses, which are used to define a two-way mapping between the GRIN Euclidean plane and a 2D curved space for the case of known refractive index distributions (Luneburg and Eaton lens) and curved surfaces (spatially modulated Gaussian profiles).

3.1 Geodesic Luneburg and Eaton Lenses

To visualize how the refractive index $n(x^1, x^2)$ can be mimicked by the geometric profile $h(x^1, x^2)$, we consider in the following the well known[2,18–20,23,36] planar Luneburg lens of Fig. 2(a). In this case, the refractive index takes the form $n = (2-(\rho/R)^2)^{1/2}$, in which R is the radius of the lens and $\rho(x^1, x^2) = [(x^1-x_c^1)^2+(x^2-x_c^2)^2]^{1/2}$ denotes the radial coordinate of the lens defined with respect to its center (x_c^1, x_c^2). To transform the planar lens into its equivalent geodesic with unit refractive index, we solve Eq. (14) numerically in terms of $h(n(x^1, x^2))$ over a circular domain of radius R with the Dirichlet boundary condition $h(\rho = R) = 0$. Fig. 2(a) shows the wavefield with wavelength $\lambda = R/10$ generated by a monopole source located on a boundary point of the lens, while Fig. 2(b) shows the corresponding wavefield on a curved surface obtained by solving Eq. (14) in Comsol Multiphysics 5.5.[37] It is noted that this surface corresponds to that found in Refs. 19, 23, where the rotational symmetry of the lens is exploited.

The interesting case of a 180° Eaton lens[38] ($n = (2R/\rho - 1)^{1/2}$) is also reported in Fig. 2(c), which shows the wavefield with $\lambda = R/10$ bending around the center of the lens, where Eq. (14) is not defined since $n(\rho = 0) = \infty$

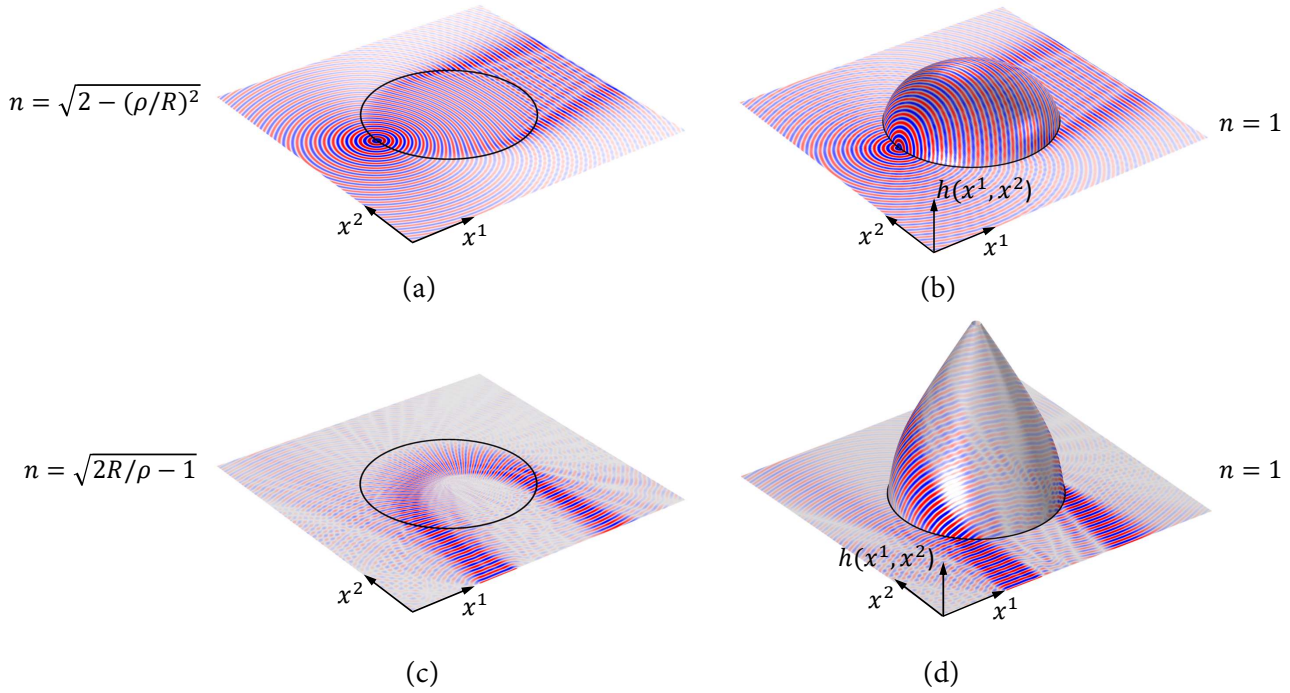

Figure 2. (a) Planar Luneburg lens and (b) its geodesic equivalent. (c) Planar 180° Eaton lens and (d) its geodesic equivalent. The indicated wavefield are for $\lambda = R/10$. For each lens, the radial coordinate is given by $r = [(x^1 - x_c^1)^2 + (x^2 - x_c^2)^2]^{1/2}$, where (x_c^1, x_c^2) are the coordinates of the center of the lens.

and the Gaussian curvature presents a singularity. To remove this singularity, we introduce a small sink at the center of the computational domain where $K(x^1, x^2) \to 0$. With this modification, the geodesic equivalent of the planar lens can be found from Eq. (14) by setting $h(\rho = R) = 0$. The corresponding surface shape is shown in Fig. 2(d), which resembles that presented in Ref. 18.

3.2 Spatially Modulated Gaussian Profiles

In Section 3.1, we demonstrated that Eq. (14) can be used to determine the geometric profile $h(x^1, x^2)$ of a geodesic lens from a given refractive index distribution $n(x^1, x^2)$ defined on the Euclidean plane x^1, x^2. In this Section, we follow the inverse process by considering the two spatially modulated Gaussian profiles $M1$ and $M2$ shown in Figs. 3(a,d), respectively, which are defined by the equations

$$M1: \quad h(x^1, x^2) = 0.006 \exp\left(-\frac{1}{2}\frac{(x^1)^2 + (x^2)^2}{0.00508^2}\right) \text{ (m)}, \tag{15}$$

$$M2: \quad h(x^1, x^2) = 0.85 \left(\frac{(x^1)^2 - (x^2)^2}{0.00889}\right) \exp\left(-\frac{1}{2}\frac{(x^1)^2 + (x^2)^2}{0.00889^2}\right) \text{ (m)}. \tag{16}$$

To demonstrate how the wave behavior for these profiles can be mimicked on a flat space, we solve Eq. (14) numerically, in which the term on the right hand side of the equation is now known. The computed refractive index maps $S1$ and $S2$ corresponding to the two waveguides $M1$ and $M2$ are shown in Figs. 3(c,f), respectively. These maps are computed by considering a circular computational domain of radius $R = 0.15$ m, which implies that $K(R) \approx 0$ on the boundary of the domain. This, in turn, allows to solve Eq. (14) numerically with the simple Dirichlet boundary condition $n(R) = 1$.

Figs. 3(c,f) also report the ray trajectories generated from a fixed point source located at about 7.6 mm above the center of the modulated Gaussian profiles, which were obtained by solving Eq. (9) using the numerical integration scheme described in Ref. 31. As it can be observed, the ray trajectories are in very good agreement with the geodesic lines on the two waveguides $M1$ and $M2$ shown in Figs. 3(b,e), respectively, which were computed using the numerical method described in Ref. 39.

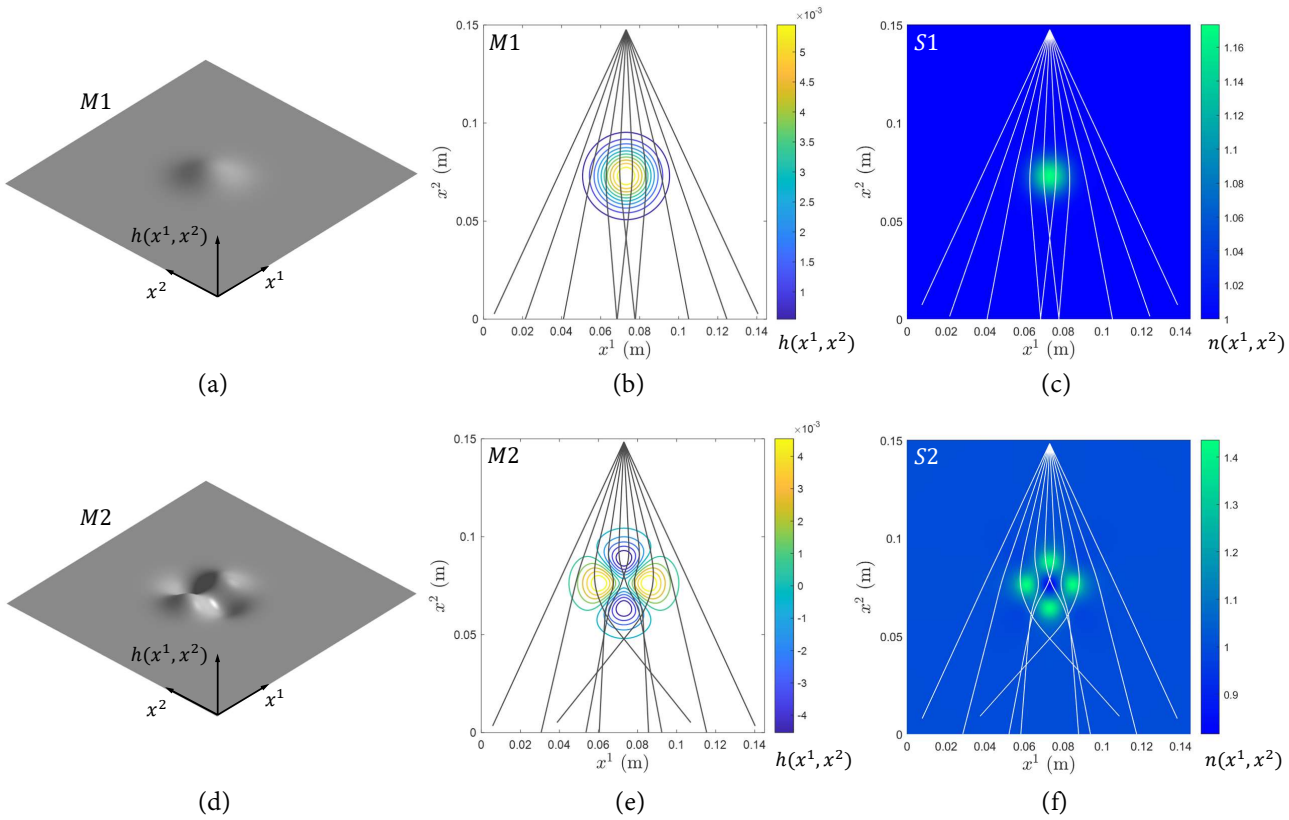

Figure 3. (a) Gaussian profile $M1$ (Eq. (15)) with (b) geodesic lines and (c) equivalent refractive index map $S1$ with ray trajectories. (d) Gaussian profile $M2$ (Eq. (16)) with (e) geodesic lines and (f) equivalent refractive index map $S2$ with ray trajectories.

4. EXPERIMENTAL ANALYSIS OF THIN CURVED WAVEGUIDES

In this Section, we study the waveguiding effects of 3D printed waveguides corresponding to the profiles $M1$ and $M2$ of Eqs. (15) and (16), respectively. Specifically, we demonstrate that the focal points of Lamb waves measured experimentally match the distribution of caustic lines formed by geodesics and ray trajectories in accordance to the numerical analysis of Sections 2.1 and 3.2.

4.1 Experimental Setup

The 3D printed waveguides $M1$ and $M2$ are shown in Figs. 4(a,b), respectively, and were fabricated with a thickness of 1.27 mm using Aluminum filled Nylon 12. Lamb waves were generated in the waveguides by means of a piezoelectric disks installed at the same location of the source point shown in Figs. 3(b,e). The piezoelectric disks were excited through the internal function generator of a Polytec PSV-500 Xtra scanning laser Doppler vibrometer (SLDV), which was also used to record the transverse velocity component $v(x^1, x^2, t)$. The source signal is a chirp of the form

$$F(t) = w(t) \sin\left(2\pi f_0 t + \frac{\pi B t^2}{T}\right), \tag{17}$$

with amplitude $w(t) = 0.5$ V (amplified with 55 dB gain), starting frequency $f_0 = 35$ kHz, frequency bandwidth $B = 265$ kHz and chirp duration $T = 0.2$ ms, while the total length of the recorded signal is 4.00 ms. The velocity arrays $v(x^1, x^2, t)$ were recorded over a rectangular area (dashed lines in Fig. 4) with a sampling frequency of 1.25 MHz, a 250 Hz repetition rate and a 5% pre-triggering. Each waveform was averaged 100 times in order to maximize the signal-to-noise ratio. The rectangular area was scanned by considering a grid with a spatial step of 0.9 mm.

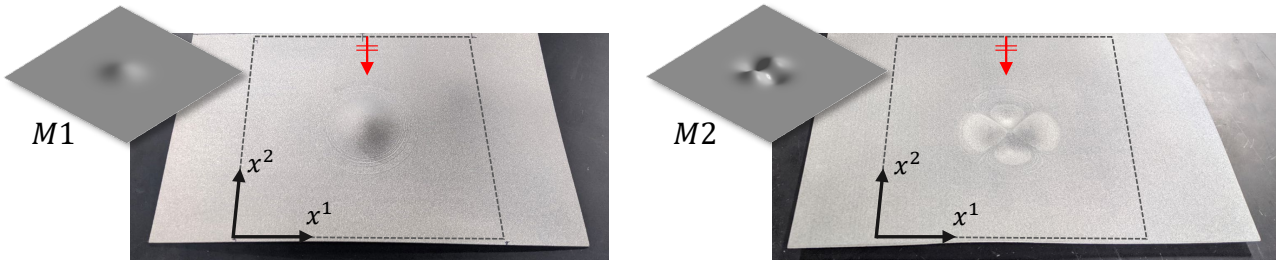

(a) (b)

Figure 4. (a) 3D printed waveguide of the Gaussian profile $M1$ (Eq. (15)) and (b) $M2$ (Eq. (16)). The dashed line indicates the boundary of the SLDV scan area, while the arrow denotes the direction of the incident Lamb modes.

The recorded velocity arrays $v(x^1, x^2, t)$ were post-processed by applying a filter in the frequency and wavenumber domain such that only the fundamental A_0 Lamb mode was retained for the analysis in the $100-300$ kHz range. In this range, the wavelength of the A_0 mode was found to span from 2.75 mm to 5.7 mm, which ensures that the hypotheses of Section 2.1 are not violated.

4.2 Results and Discussion

The results obtained from the experimental and numerical analyses of Sections 4.1 for the waveguides $M1$ and $M2$ are shown in Figs. 5(a,b), respectively.

For the waveguide $M1$, a time snapshot of the filtered experimental velocity field $v(x^1, x^2, t)$ measured with the SLDV is reported in the top view of Fig. 5(a). As it can be observed, the circular wavefronts formed by the A_0 mode undergo some distortion while crossing the Gaussian dome, which behaves similarly to a Luneburg lens, although with a different radial variation of the refractive index. This difference translates into an elongated focal line below the center of the dome, which can be clearly observed in the normalized Root Mean Square (RMS) map of the velocity field (middle view of Fig. 5(a)). In this map, the continuous lines indicate the loci of zero Gaussian curvature, while the $+$ and $-$ symbols indicate regions of positive and negative Gaussian curvature, respectively. In the bottom view of Fig. 5(a), the geodesic lines are superimposed to the RMS map, from which it can be inferred that the caustic network predicts the location and extension of the focal region with good accuracy.

The velocity field and RMS maps of the waveguide $M2$ (top and middle view of Fig. 5(b), respectively) indicate a more complex behavior of the circular wavefronts when these cross the spatially modulated Gaussian dome. In particular, it can be observed from the RMS plot how two main focal lines depart from the center of the dome, where $K(x^1, x^2) < 0$, and closely follow the virtual contours corresponding to $K(x^1, x^2) = 0$. This behavior can be qualitatively interpreted in terms of Fermat's principle, based on which caustics will tend to form on regions where the space is locally flat, thus minimizing their time of flight between two locally close points. Also in this case, it can be observed from the bottom view of Fig. 5(b) that the caustic networks formed by the geodesics closely match the regions of high wave amplitude observable in the experimental RMS map.

Overall, the experimental results presented in this Section confirm that the geodesic and ray theories can provide an accurate estimation of the waveguiding effects in curved two-dimensional spaces when operating within the geometrical optics limits.

5. CONCLUSIONS

We demonstrated that waveguiding effects for flexural elastic waves propagating in thin, isotropic, curved waveguides can be studied, in the short wavelength limit, by means of the classical equation of geodesics. Moreover, a non-Euclidean transformation that establishes the geometric equivalence between a curved 2D space and a planar refractive index distribution has also been proposed, which was used to design geodesic Luneburg and Eaton lenses from their planar counterparts. Spatially modulated Gaussian profiles with a generic curvature distribution were also investigated. In this case, numerical analyses demonstrated that their curvature-induced

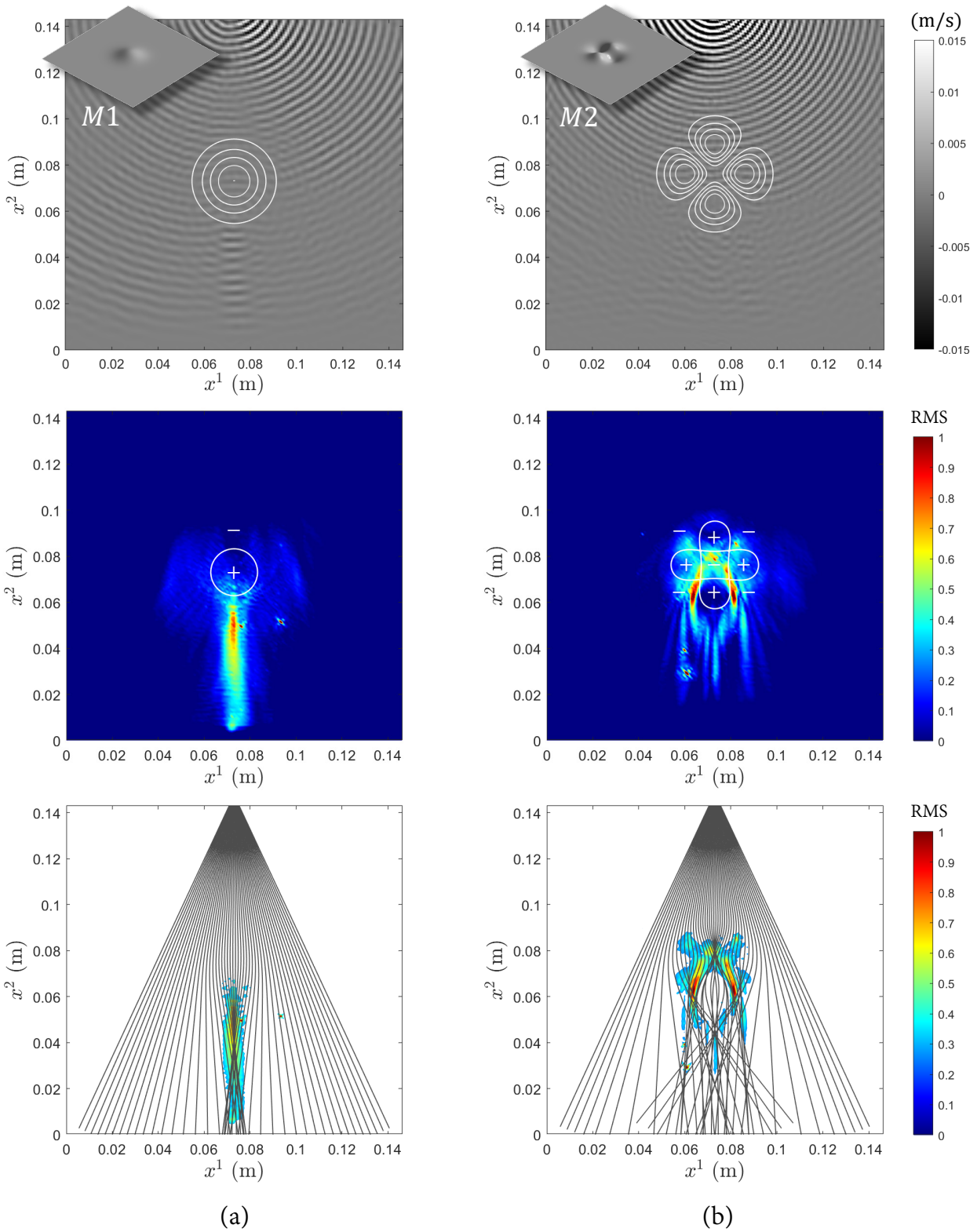

Figure 5. Experimental results for the 3D printed waveguides (a) $M1$ (Eq. (15)) and (b) $M2$ (Eq. (16)). Top view: snapshot of the filtered A_0 Lamb mode. Middle view: normalized Root Mean Square (RMS) of the velocity field with contour lines of zero Gaussian curvature. Bottom view: geodesic lines superimposed to the normalized RMS.

waveguiding effects can be equivalently evaluated by geodesic and ray analysis, while experimental tests performed on 3D printed waveguides confirmed that the focal points and lines formed by A_0 Lamb modes coincide with the numerically computed caustic networks.

Being based on purely geometric arguments, the proposed theoretical framework can also be extended to problems of geometrical optics, and opens up to the possibility of realizing geodesic lenses that can overcome the problems typically encountered in flat metamaterial-based lens design, where the realization of complex gradient index profiles is limited by material properties and manufacturing processes.

REFERENCES

[1] McCall, M., Pendry, J. B., and et al., V. G., "Roadmap on transformation optics," *Journal of Optics* **20**, 063001 (may 2018).

[2] Mitchell-Thomas, R. C. and Quevedo-Teruel, O., [*Transformation Optics Applied to Antennas and Focusing Systems*], 387–406, Springer International Publishing, Cham (2018).

[3] Pendry, J. B., Schurig, D., and Smith, D. R., "Controlling electromagnetic fields," *Science* **312**(5781), 1780–1782 (2006).

[4] Leonhardt, U., "Optical conformal mapping," *Science* **312**(5781), 1777–1780 (2006).

[5] Padilla, W. J., Basov, D. N., and Smith, D. R., "Negative refractive index metamaterials," *Materials Today* **9**(7), 28–35 (2006).

[6] Schurig, D., Mock, J. J., Justice, B. J., Cummer, S. A., Pendry, J. B., Starr, A. F., and Smith, D. R., "Metamaterial electromagnetic cloak at microwave frequencies," *Science* **314**(5801), 977–980 (2006).

[7] Valentine, J., Zhang, S., Zentgraf, T., Ulin-Avila, E., Genov, D. A., Bartal, G., and Zhang, X., "Three-dimensional optical metamaterial with a negative refractive index," *Nature* **455**, 376–379 (2008).

[8] Alitalo, P. and Tretyakov, S., "Electromagnetic cloaking with metamaterials," *Materials Today* **12**(3), 22–29 (2009).

[9] Chen, H., Chan, C., and Sheng, P., "Transformation optics and metamaterials," *Nature Materials* **9**, 387–396 (2010).

[10] Zhang, B., "Electrodynamics of transformation-based invisibility cloaking," *Light Sci Appl* **1**, e32 (2012).

[11] Sun, F., Zheng, B., Chen, H., Jiang, W., Guo, S., Liu, Y., Ma, Y., and He, S., "Transformation optics: From classic theory and applications to its new branches," *Laser & Photonics Reviews* **11**(6), 1700034 (2017).

[12] Wang, H., Deng, Y., and Zheng, B. e. a., "Panoramic lens designed with transformation optics," *Scientific Reports* **7**, 40083 (2017).

[13] Rinehart, R. F., "A solution of the problem of rapid scanning for radar antennae," *Journal of Applied Physics* **19**(9), 860–862 (1948).

[14] Rinehart, R. F., "A family of designs for rapid scanning radar antennas," *Proceedings of the IRE* **40**(6), 686–688 (1952).

[15] Righini, G. C., Russo, V., Sottini, S., and di Francia, G. T., "Geodesic lenses for guided optical waves," *Appl. Opt.* **12**, 1477–1481 (Jul 1973).

[16] Southwell, W. H., "Geodesic optical waveguide lens analysis," *J. Opt. Soc. Am.* **67**, 1293–1299 (Oct 1977).

[17] Sochacki, J., "Perfect geodesic lens designing," *Appl. Opt.* **25**, 235–243 (Jan 1986).

[18] Šarbort, M. and Tyc, T., "Spherical media and geodesic lenses in geometrical optics," *Journal of Optics* **14**, 075705 (jul 2012).

[19] Mitchell-Thomas, R. C., Quevedo-Teruel, O., McManus, T. M., Horsley, S. A. R., and Hao, Y., "Lenses on curved surfaces," *Opt. Lett.* **39**, 3551–3554 (Jun 2014).

[20] Horsley, S., Hooper, I., Mitchell-Thomas, R., and Quevedo-Teruel, O., "Removing singular refractive indices with sculpted surfaces," *Sci Rep* **4**, 4876 (2014).

[21] Miñano, J. C., Benítez, P., and González, J. C., "Perfect imaging with geodesic waveguides," *New Journal of Physics* **12**, 123023 (dec 2010).

[22] Xu, L., Tyc, T., and Chen, H., "Conformal optical devices based on geodesic lenses," *Opt. Express* **27**, 28722–28733 (Sep 2019).

[23] Liao, Q., Fonseca, N. J. G., and Quevedo-Teruel, O., "Compact multibeam fully metallic geodesic luneburg lens antenna based on non-euclidean transformation optics," *IEEE Transactions on Antennas and Propagation* **66**(12), 7383–7388 (2018).
[24] Fonseca, N. J. G., Liao, Q., and Quevedo-Teruel, O., "Equivalent planar lens ray-tracing model to design modulated geodesic lenses using non-euclidean transformation optics," *IEEE Transactions on Antennas and Propagation* **68**(5), 3410–3422 (2020).
[25] Evans, A. A. and Levine, A. J., "Reflection and refraction of flexural waves at geometric boundaries," *Phys. Rev. Lett.* **111**, 038101 (Jul 2013).
[26] Zhu, J., Liu, Y., Liang, Z., Chen, T., and Li, J., "Elastic waves in curved space: Mimicking a wormhole," *Phys. Rev. Lett.* **121**, 234301 (Dec 2018).
[27] Norris, A. N. and Rebinsky, D. A., "Membrane and Flexural Waves on Thin Shells," *Journal of Vibration and Acoustics* **116**, 457–467 (10 1994).
[28] Norris, A. N., "Rays, beams and quasimodes on thin shell structures," *Wave Motion* **21**(2), 127–147 (1995).
[29] Martino, V., "On the characteristic curvature operator," *Communications on Pure & Applied Analysis* **11**(5), 1911–1922 (2012).
[30] Hayashi, T., Kawashima, K., Sun, Z., and Rose, J. L., "Guided wave propagation mechanics across a pipe elbow," *ASME. J. Pressure Vessel Technol.* **127(3)**, 322–327 (2005).
[31] Sharma, A., Kumar, D. V., and Ghatak, A. K., "Tracing rays through graded-index media: a new method," *Appl. Opt.* **21**(6), 984–987 (1982).
[32] Leonhardt, U. and Philbin, T., [*Geometry and light, The Science of Invisibility*], Dover Publications, Inc. (2010).
[33] Carmo, M., [*Differential Geometry of Curves and Surfaces*], Prentice-Hall, Inc., Englewood Cliffs, New Jersey, USA (1976).
[34] Kamien, R. D., Nelson, D. R., Santangelo, C. D., and Vitelli, V., "Extrinsic curvature, geometric optics, and lamellar order on curved substrates," *Phys. Rev. E* **80**, 051703 (Nov 2009).
[35] Kropla, W. C. and Lehn, W. H., "Differential geometric approach to atmospheric refraction," *J. Opt. Soc. Am. A* **9**, 601–608 (Apr 1992).
[36] Doric, S. and Munro, E., "General solution of the non-full-aperture luneburg lens problem," *J. Opt. Soc. Am.* **73**, 1083–1086 (Aug 1983).
[37] "Comsol multiphysics 5.5, https://www.comsol.com," (2020).
[38] Kim, S.-H., "Retroreflector approximation of a generalized eaton lens," *Journal of Modern Optics* **59**(9), 839–842 (2012).
[39] Burazin, A., [*Calculating geodesics on surfaces*], McMaster University (2008).